

₁ Space-Time Ambiguity Function in 3-D ISR

John Swoboda,¹ Joshua Semeter,¹ Philip Erickson²

Corresponding author: J. P. Swoboda, Department of Electrical & Computer Engineering,
Boston University, 8 Saint Marys Street Boston, MA 02215, USA. (swoboj@bu.edu)

¹Department of Electrical & Computer
Engineering, Boston University, Boston,
Massachusetts, USA.

²Atmospheric Science Division, MIT
Haystack Observatory, Westford
Massachusetts, USA.

By leveraging electronically steerable phased array antenna technology, incoherent scatter radars (ISR) have now become full three-dimensional remote sensors for ionosphere plasmas. Currently these systems are operating in the high latitude region where the ionosphere is highly dynamic in both space and time. Because of the highly dynamic nature of the ionosphere in this region it is important to differentiate between artifacts and the true behavior of the plasma. Often the three dimension data is fitted in a spherical coordinate space and then the parameters are interpolated to a Cartesian grid. This and other sources of error could be impacting the reconstructions of the plasma parameters.

In this study we present a new way of analyzing 3-D dimension ISR through use of the space-time ambiguity function. This concept is similar to the range ambiguity function that is used in traditional ISR for scanning antenna systems but has been extended to all spatial dimension along with time as well.

The use of this new ambiguity function allow us to pose this problem in terms of a linear inverse problem for the lags of the intrinsic plasma autocorrelation function. From this we can explore the impact of non-stationarity in the plasma parameters in both time and space. Along with showing possible artifacts we will begin to explore ways of reducing these artifacts.

1. Introduction

Incoherent scatter radar (ISR) systems have enabled researchers since the 1950's to explore the ionosphere [Gordon, 1958]. Using methodology developed by Dougherty, Farley and others these systems can give measurements of electron density N_e , Ion temperature T_i , electron temperature T_e , Ion velocity V_i and other plasma parameters [Dougherty and Farley, 1960; Farley et al., 1961; Dougherty and Farley, 1963; Hagfors, 1961]. These parameters are measured by fitting a nonlinear theoretic autocorrelation function (ACF) model derived from first principles physics to an estimated intrapulse time autocorrelation of the scattered radar signal [Lehtinen and Huuskonen, 1996].

As with any real world measurement method there is limit to the spatial and temporal resolution of ISR systems. This resolution is determined by the ability of the sensor to create independent measurements of the ACF in time and space of what is essentially a zero-mean complex Gaussian process. At space and time extents smaller than these resolutions the random process that the ACF is derived from is assumed to be stationary. In ISR literature the ambiguity function encapsulates the spatial resolution in the range dimension. This ambiguity emerges as a function of range and correlation lag due to the pulse modulation and the finite bandwidth of the receiver [Farley, 1969]. The time resolution is determined by how long it takes to average the autocorrelation function to reduce the variance of the estimate to a desired level.

This assumption of stationarity at the level of the ambiguity function constrains the measurement and creates a blurring and other forms of artifacts due to the non-linear fitting of plasma parameters. In order to reduce the impact of these ambiguities a number techniques have been developed. Some techniques include trying to reduce the extent of the ambiguity function by adjusting the waveform. Barker code wave forms are used in ISR but mainly for low altitude studies of the E-region due to the inability to form a spectrum from them. Another method for reducing the ambiguity in range is using alternating codes [*Gray and Farley, 1973; Lehtinen and Haggstrom, 1987; Sulzer, 1993; Sulzer, 1989*].

Another set of techniques often shown in the literature focus on reducing the impact of the ambiguity function through post processing. The first method, full profile analysis, consists of fitting physical parameter values to entire range extent taking into account all of the correlations between all locations [*Holt et al., 1992; Lehtinen, 1989; Lehtinen et al., 1997; Hysell et al., 2008*]. This technique often places constraints on the physical parameters as in *Hysell et al. [2008]*. Because the the relationship between the autocorrelation function and the lags are non-linear this method often yields algorithms that require a large amount computation to calculate the covariance matrices between all of the values.

The other set of post processing methods, such as in *Nikoukar et al. [2008]* and *Virtanen et al. [2008]*, treat the problem as a linear inverse problem of the lags. Methods such as total-variations or Tikhonov regularization can be applied to the lags to try to fill in the missing information nation from the null space of the operator.

These methods are easy to compute and can rely on a large body of knowledge from engineering communities that study linear inverse problems.

Recently phased array technology has started to be leveraged by ISR community. The Advance Modular Incoherent Scatter Radar (AMISR) systems have already been deployed both at the Poker Flat Alaska (PFISR) and Resolute Bay Canada (RISR) [ami, 2014]. The EISCAT-3D project is currently being developed using phased array technology as well and will be capable of multistatic processing [eis, 2005]. These new systems are already being used to create three dimensional reconstructions of plasma parameters [Semeter et al., 2009], [Nicolls and Heinselman, 2007; Dahlgren et al., 2012a, b].

There has been no formal derivation of an ambiguity function for all three spatial dimensions for these systems, although up until recently ISR systems, which only had dish antennas, could not mitigate the finite beam width effects. In a highly dynamic region like the high latitude ionosphere this lack of knowledge can be problematic. There are numerous phenomena such as polar cap patches that may be moving through the field of view at very high speeds [Dahlgren et al., 2012a]. This motion can cause an apparent expansion in the shape of the beams if one represents the beams in the frame of reference of the moving plasma.

These three-dimensional reconstructions often consist of taking the fitted parameters and then interpolating them to a Cartesian space from the system's natural spherical coordinate space [Butler, 2013]. The step of fitting the autocorrelation function to the theoretical functions to find the final plasma parameters is a non-

linear operation. Because of this it is impossible to exactly predict the impact on the parameter values as different plasma populations move through the field of view of the radar. Alternatively it is possible to treat the formation of the autocorrelation estimates as a linear process with each lag as an independent channel [Nikoukar et al., 2008].

Using this methodology we can make many parallels between ISR and CCD cameras. In cameras blurring can take place when an object moves over a space covered by one pixel while the shutter is open and the CCD is collecting photons. A diagram of this can be seen in Figure 1. The same holds for ISR except that the pixels are no longer square and instead are determined by the beam shape and pulse pulse pattern. This is shown in the diagrams in Figure 2.

In this publication we will develop a model for a full three dimensional space-time ambiguity function for 3-D ISR systems. This function can also be modified to show the ambiguity within the rest frame of the moving plasma. In the end this full three dimensional can be represented as kernel in a Fredholm integral equation like in Equation 1 with $f(s)$ being the lag of the autocorrelation function at a specific time and position.

$$g(t) = \int_a^b K(t, s) f(s) ds \quad (1)$$

The impact of the three-dimensional ambiguity on moving plasma will be shown through simulation. This ISR simulator fully emulates the ISR data creation process at the IQ level.

Lastly possible mitigation techniques will be explored. These mitigation techniques will borrow heavily from the image and signal processing literature.

2. Space-Time Ambiguity

The three dimensional nature of the problem requires first defining the spatial coordinate system, $\mathbf{r} = [x, y, z]^T$. For this coordinate system, $\mathbf{r} = [0, 0, 0]^T$ at the location of the radar and thus $r = |\mathbf{r}|$, also known as the range variable. This allows for the use of polar coordinates $\mathbf{r} = [r, \theta, \phi]^T$ where θ is the physical elevation angle, ϕ is the physical azimuth angle.

The radar will sample this space into a set of discrete points which will be referred to as $\mathbf{r}_s = [x_s, y_s, z_s]^T$ along with the discretized range $r_s = |\mathbf{r}_s|$. The sampled space will consist of a number of points which are the combinations of the range gates and number of beams. This points can also be referred in the polar coordinates $\mathbf{r}_s = [r_s, \theta_s, \phi_s]^T$, where θ_s is the sampled elevation angle, ϕ_s is the sampled azimuth angle.

For notation purposes we use two different sets of time commonly known in radar literature as fast-time, n and slow-time, t [Richards, 2005].. Fast-time is used to explore the workings of the radar on the order of the radar systems A/D conversion such as lag formation. Slow-time will used for processes that vary in time on the order of the system's pulse repetition interval (PRI). In order to form estimates of the ACFs, with desired statistical properties, it is assumed that the plasma parameters parameters will change on the order of 10 to hundreds of PRIs. The term n will

be a sampled parameter while t will represent a continuous time and t_s will be the slow time parameter sampled by the radar. The sampling of t_s can at lowest be the PRI but generally it is sampled once in an integration period so the reconstructed parameters can be considered as independent measurements in time.

2.1. Derivation

The basic physical mechanism behind ISR is that electron density fluctuations in the ionosphere, $n_e(\mathbf{r}, n)$, scatter radio waves which can be observed by the receiver system of the radar [Hysell et al., 2008]. The emitted radar signal will have a pulse shape $s(n)$ modulated at a central frequency that results in a scattering wave number \mathbf{k} . Using the Borne approximation the signal received at time n , $x(n)$, can be represented as the following

$$x(n) = h(n) * \int e^{-j\mathbf{k}\cdot\mathbf{r}} s\left(n - \frac{2r}{c}\right) n_e(\mathbf{r}, n) d\mathbf{r}, \quad (2)$$

where $h(n)$ is the receiver filter. In modern ISR systems this signal $x(n)$ is then sampled at discrete points in fast-time which will be referred to as n_s . The convolution and sampling operation can be brought in the integral as the following,

$$x(n_s) = \int e^{-j\mathbf{k}\cdot\mathbf{r}} s\left(n - \frac{2r}{c}\right) n_e(\mathbf{r}, n) h(n_s - n) d\mathbf{r} dn \quad (3)$$

Once the signal has been received and sampled the autocorrelation function is then to be estimated from the sampled signal $x(n_s)$. The full expression of the underlying autocorrelation of this signal is the following,

$$\langle x(n_s)x^*(n'_s) \rangle = \int e^{-j\mathbf{k} \cdot (\mathbf{r}' - \mathbf{r})} s\left(n - \frac{2r}{c}\right) s^*\left(n' - \frac{2r'}{c}\right) h(n_s - n)h(n'_s - n') \langle n_e(\mathbf{r}, n)n_e^*(\mathbf{r}', n') \rangle d\mathbf{r}d\mathbf{r}'dn dn', \quad (4)$$

141 where r' is the magnitude of the vector \mathbf{r}' . By assuming stationarity of the second
 142 order statistics of the signal along fast time, we can substitute the in the lag variables
 143 $\tau \equiv n' - n$, and $\tau_s \equiv n'_s - n_s$. With these substitutions Equation 4 becomes

$$\langle x(n_s)x^*(n_s + \tau_s) \rangle = \int e^{-j\mathbf{k} \cdot (\mathbf{r}' - \mathbf{r})} s\left(n - \frac{2r}{c}\right) s^*\left(n + \tau - \frac{2r'}{c}\right) h(n_s - n)h(n_s + \tau_s - n - \tau) \langle n_e(\mathbf{r}, n)n_e^*(\mathbf{r}', n + \tau) \rangle d\mathbf{r}d\mathbf{r}'dn d\tau \quad (5)$$

144 We can make a simplifying assumption at this point that the space-time autocorre-
 145 lation function of $n_e(\mathbf{r}, t)$, $\langle n_e(\mathbf{r}, n)n_e(\mathbf{r}', n + \tau) \rangle$, will go to zero as the magnitude of
 146 $\mathbf{x} \equiv \mathbf{r}' - \mathbf{r}$ increases. The rate that the space-time autocorrelation goes to zero will
 147 be such that $\tau \gg \frac{2\|\mathbf{x}\|}{c}$ thus in the argument of the pulse shape $r \approx r'$. This allows
 148 Equation 5 to be rewritten as

$$\langle x(n_s)x^*(n_s + \tau_s) \rangle = \int s\left(n - \frac{2r}{c}\right) s^*\left(n + \tau - \frac{2r}{c}\right) h(n_s - n)h^*(n_s + \tau_s - n - \tau) \left[\int e^{-2j\mathbf{k} \cdot \mathbf{x}} \langle n_e(\mathbf{r}, n)n_e^*(\mathbf{x} + \mathbf{r}, n + \tau) \rangle d\mathbf{x} \right] d\mathbf{r}dn d\tau. \quad (6)$$

The inner integral is a spatial Fourier transform evaluated at the wave number of the radar \mathbf{k} . By again asserting stationary along slow time we can represent the true

ACF as the following,

$$R(\tau, \mathbf{r}) = \langle |n_e(\mathbf{k}, r, \tau)|^2 \rangle \equiv \int_{\mathbf{x}} e^{-2j\mathbf{k} \cdot \mathbf{x}} \langle n_e(\mathbf{r}, b) n_e^*(\mathbf{x} + \mathbf{r}, n + \tau) \rangle d\mathbf{x}. \quad (7)$$

Now Equation 6 becomes

$$\langle x(n_s) x^*(n_s + \tau_s) \rangle = \int \langle |n_e(\tau, \mathbf{k}, \mathbf{r})|^2 \rangle \left[\int s\left(n - \frac{2r}{c}\right) s^*\left(n + \tau - \frac{2r}{c}\right) h(n_s - n) h^*(n_s + \tau_s - n - \tau) dn \right] d\tau dr. \quad (8)$$

If n_s is replaced with $2r_s/c$ we can introduce the range ambiguity function $W(\tau_s, r_s, \tau, r)$ by doing the following substitution,

$$W(\tau_s, r_s, \tau, r) = \int s\left(n - \frac{2r}{c}\right) s^*\left(n + \tau - \frac{2r}{c}\right) h\left(2r_s/c - n\right) h^*\left(2r_s/c + \tau_s - n - \tau\right) dn. \quad (9)$$

Assuming, for the moment, that $R(\tau, \mathbf{r})$ only varies across the range dimension r we can now represent this in the form of a Fredholm integral equation

$$\langle x(2r_s/c) x^*(2r_s/c + \tau_s) \rangle = \int W(\tau_s, r_s, \tau, r) R(\tau, r) dr d\tau. \quad (10)$$

The range ambiguity function, $W(\tau_s, r_s, \tau, r)$, can be thought of as a smoothing operator along the range and lag dimensions of $R(\tau, r)$.

The spatial ambiguity across angle is determined by the antenna beam pattern. In phase array radars this beam pattern is ideally the array factor multiplied by the element pattern [Balanis, 2005]. The array factor is determined by a number of things including the element spacing in both x and y (dx, dy) and the wave number of the radar, k . Making idealized assumptions with no mutual coupling and that the array elements are cross dipole elements AMISR systems will have the following

antenna pattern for pointing angle (θ_s, ϕ_s) ,

$$F(\theta_s, \phi_s, \theta, \phi) = \frac{1}{2}(1 + \cos(\theta)^2) \left[\frac{1}{MN} (1 + e^{j(\psi_y/2 + \psi_x)}) \frac{\sin((M/2)\psi_x)}{\sin(\psi_x)} \frac{\sin((N/2)\psi_x)}{\sin(\psi_x/2)} \right]^2, \quad (11)$$

where $\psi_x = -kd_x(\sin \theta \cos \phi - \sin \theta_s \cos \phi_s)$, $\psi_y = -kd_y(\sin \theta \sin \phi - \sin \theta_s \sin \phi_s)$ and M is the number of elements in the x direction of the array N is the number of elements in the y direction(see Appendix: A for derivation).

This spatial ambiguity is a separable function made up of the components of $W(\tau_s, \tau, r_s, r)$ and $F(\theta_s, \phi_s, \theta, \phi)$. These two functions can be combined by multiplying the two, creating the spatial ambiguity function $K(\tau_s, \mathbf{r}_s, \tau, \mathbf{r})$, and then doing a volume integration. This will create radar system's estimate of the ACF with one pulse which will be referred to as $\rho(\tau_s, \mathbf{r}_s)$,

$$\rho(\tau_s, \mathbf{r}_s) = \int F(\theta_s, \phi_s, \theta, \phi) W(\tau_s, r_s, \tau, r) R(\tau, \mathbf{r}) dV, \quad (12)$$

$$= \int K(\tau_s, \mathbf{r}_s, \tau, \mathbf{r}) R(\tau, \mathbf{r}) dV. \quad (13)$$

A rendering of an example of this full ambiguity function for an uncoded long pulse and antenna pattern in Equation 11 for four beams can be seen in Figure 3.

This one pulse is a single sample of a random process. In order to create a usable estimate numerous instances of this ACF need to be averaged together to reduce the variance in order to fit the estimate to a theoretical ACF that is tied to plasma parameter values. To show the impact of this averaging to create the estimate of the ACF we will add slow-time dependence to $R(\tau, \mathbf{r}, t)$ along with another separable

function $G(t_s, t)$ to the kernel. This function $G(t_s, t)$, while reducing the variance can create blurring of the ACF if the plasma parameters change within a non-coherent processing interval. Since the radar is sampling the space with individual pulses this function can take the form of a summation of dirac delta functions

$$G(t_s, t) = \sum_{j=0}^J \alpha_j \delta(t - t_s - jT_{PRI}), \quad (14)$$

where J is the number of pulses used over a non-coherent processing interval, T_{PRI} is the PRI time period and α_j is the weights that the radar assigns to the pulses. The weights are generally set to $1/J$ to simply average the pulses. With Equation 14 incorporated into the overall ambiguity we see the full integral equation,

$$\rho(\tau_s, \mathbf{r}_s, t_s) = \int G(t_s, t) K(\tau_s, \mathbf{r}_s, \tau, \mathbf{r}) R(\tau, \mathbf{r}, t) dV dt \quad (15)$$

$$\rho(\tau_s, \mathbf{r}_s, t_s) = \int L(\tau_s, \mathbf{r}_s, t_s, \tau, \mathbf{r}, t) R(\tau, \mathbf{r}, t) dV dt. \quad (16)$$

The final kernel, $L(\tau_s, \mathbf{r}_s, t_s, \tau, \mathbf{r}, t)$ encompasses the full space-time ambiguity.

2.2. Ambiguity after Frame Transformation

We will now focus on the impact of the motion of plasma as it is going through the field of view of the radar. We will assume that the radar is integrating over a length of time T beginning at t_s . The kernel L will be represented as a separable function K and G as in Equation 15. In this case G will be an indicator function of length T and centered at $t_0 + 1/2$. This will change Equation 15 to the following,

$$\rho(\tau_s, \mathbf{r}_s, t_s) = \int K(\tau_s, \mathbf{r}_s, \tau, \mathbf{r}) \left[\int_{t_s}^{t_s+T} R(\tau, \mathbf{r}, t) dt \right] dV. \quad (17)$$

Of specific interest are instances in the high latitude ionosphere where embedded plasma structures are moving due to the electric field of the magnetosphere. Because of this it will be assumed that the plasma is rigid object and will not deform with respect to \mathbf{r} over time period $[t_0, t_0 + T]$. Also it will be assumed that it will be moving with a constant velocity \mathbf{v} . Thus $R(\tau, \mathbf{r}, t) \Rightarrow R(\tau, \mathbf{r} + \mathbf{v}t)$. At this point Equation 17 becomes,

$$\rho(\tau_s, \mathbf{r}_s, t_s) = \int \int_{t_s}^{t_s+T} K(\tau_s, \mathbf{r}_s, \tau, \mathbf{r}) R(\tau, \mathbf{r} + \mathbf{v}t) dt dV \quad (18)$$

A change of variables where $\mathbf{r}' = \mathbf{r} + \mathbf{v}t$ acts as a Galilean transform and applies a warping to the kernel and changing the frame of reference. Then Equation 18 becomes

$$\rho(\tau_s, \mathbf{r}_s, t_s) = \int \int_{t_s}^{t_s+T} K(\tau_s, \mathbf{r}_s, \tau, \mathbf{r}' - \mathbf{v}t) R(\tau, \mathbf{r}') dt dV. \quad (19)$$

Since $R(\tau, \mathbf{r}')$ is no longer dependent on t Equation 19 becomes,

$$\rho(\tau_s, \mathbf{r}_s, t_s) = \int \left[\int_{t_s}^{t_s+T} K(\tau_s, \mathbf{r}_s, \tau, \mathbf{r}' - \mathbf{v}t) dt \right] R(\tau, \mathbf{r}') dV. \quad (20)$$

By performing the integration in t the problem can now be simplified further back to a Fredholm integral equation by simply replacing the terms in the square brackets as a new kernel A ,

$$\rho(\tau_s, \mathbf{r}_s, t_s) = \int A(\tau_s, \mathbf{r}_s, t_s, \tau, \mathbf{r}') R(\tau, \mathbf{r}') dV. \quad (21)$$

The impact of the plasma velocity on the ambiguity function can be seen in Figure 4. This is the same ambiguity as seen in Figure 3 but with a velocity of 500 m/s in the y direction over a period of 2 minutes. This velocity creates a larger ambiguity function in the frame of reference of the moving plasma.

The operator A can be determined through knowledge of the radar system's beam pattern along with the experiments pulse pattern, integration time and velocity of the plasma. This velocity \mathbf{v} can be estimated by taking measurements of the Doppler shift and using a methodology seen in [Butler et al., 2010]. Once the operator has been determined standard processing techniques can be used as if the plasma is not moving.

3. Simulation

In order to show the impact of the ambiguity function, synthetic data was created using a known condition of a simulated ionosphere. The simulator creates data by deriving filters from the autocorrelation function and applying it to complex white Gaussian noise. In a sense every point in time and space noise plant and filter structure as in Figure 5. The data is then scaled and summed together according to its location in range and angle space to radar.

After the IQ data has been created it is processed in to create an estimates of the ACF at desired points of space. This processing follows flow chart seen in Figure 6.

The sampled I/Q can be represented as $x(n) \in \mathbb{C}^N$ where N is the number of samples in an inter pulse period. At this point the first step in estimating the autocorrelation function is taken. For each range gate $m \in 0, 1, \dots, M-1$ an autocorrelation is estimated for each lag of $l \in 0, 1, \dots, L-1$. To get better statistics this operation is performed for each pulse $j \in 0, 1, \dots, J-1$ and then summed over the J pulses. The entire operation to form the initial estimate of $\hat{R}(m, l)$ can be seen in Equation 22:

$$\hat{R}(m, l) = \sum_{j=0}^{J-1} x(m - \lfloor l/2 \rfloor, j) x^*(m + \lceil l/2 \rceil, j). \quad (22)$$

The case shown in Equation 22 is a centered lag product, other types of lag products calculations are available but generally a centered product is used. In the centered lag product case range gate index m and sample index n can be related by $m = n - \lfloor L/2 \rfloor$ and the maximum lag and sample relation is $M = N - \lceil L/2 \rceil$.

After the lag products have been formed an estimate of the noise correlation is subtracted out of $\hat{R}(m, l)$, which is defined as $\hat{R}_w(m, l)$:

$$\hat{R}_w(m_w, l) = \sum_{j=0}^{J-1} w(m_w - \lfloor l/2 \rfloor, j) w^*(m_w + \lceil l/2 \rceil, j), \quad (23)$$

where $w(n_w)$ is the background noise process of the radar. Often the noise process is sampled during a calibration period for the radar when nothing is being emitted. The final estimate of the autocorrelation function after the noise subtraction and summation rule will be represented by $\hat{R}_f(m, l)$. At this point a summation rule is applied and the data is sent off to be fit.

In order to demonstrate the blurring taking place from the motion of plasma a phantom ionosphere is created where a small plasma enhancement moves through the radar field of view. The background electron density varies in altitude as a Chapman function while the electron and ion temperature remains constant. This can be seen in Figure 7. This is done to avoid having to do full fit and thus only try to measure the electron density. Also estimates of the zeroth lag are only necessary. Added to this is a 35 km radius sphere of enhance electron density of about $5 \times 10^{10} \text{ m}^{-3}$ centered at 400 km altitude moving at 500 m/s along the \mathbf{y} direction. Images from this phantom can be seen in Figure 8.

Using the phantom we can see how just simply changing the integration time can impact the reconstruction. In Figure 10 we can see a case were only 10 pulses are used for the reconstruction. This corresponds to an integration time of about 9 seconds using the 121 beam pattern which can be seen in Figure 9. The enhancement can be seen with concentrated energy as it moves through the field of view. The problem is that there is a high amount of variance in the reconstruction. Figure 11 shows the reconstruction with 200 pulses, 3 minute integration time. The variability has been reduced but there is a large amount of blurring of the enhancement as it moves through the field of view.

In order to give a comparison a phantom was also created with no motion. This can be seen in first pane Figure 12. An image using the same integration time as in Figure 10 for the stationary phantom is the center pane in Figure 12. Another

image using the longer integration time can be seen in right pane of Figure 12. These images show that the blurring is on the same order between both integration times.

Lastly we show results of a simulation of the plasma density enhancement through the field of view with full fitting. We again use a plasma enhancement moving through the field of view at 500 m/s but the electron and ion temperature varies with time and altitude. The background ion and electron temperature vs. height can be seen in Figure 14. As the electron density enhancement travels through the field of view the temperatures drop by the same ratio that the electron density is enhanced.

The phantoms for each parameter at approximately 402 seconds can be seen in Figure 14. The reconstruction of this field at the same time can be seen in Figure 15. The reconstruction does not seem to show the electron density enhancement even in a blurred form. This is likely due to the nonlinear nature of the fitting.

4. Possible Mitigation Techniques

There are a number of possible ways to remove the ISR operator function to the data. A relatively simply way to remove the problem is to process the data in the frame of reference of the plasma. This technique includes measuring the ion velocity of the plasma and then integrating the beams that the plasma is present in as it moves through the field of view.

In order to reconstruct the plasma parameters it is necessary to do some sort of regularization. There are two type of regularization that can be applied in this case the first is parameter based regularization, like full profile analysis, and the other

is data based regularization. The term parameter based regularization in this case means applying constraints to the physical parameters that are often determined after fitting. This requires a large amount of calculation because the fitting and constraints are done in one step. Currently full profile analysis has only been applied along the range dimension and not in all three spatial dimensions. Extending this to three dimensions may make these algorithms computationally infeasible.

Data based regularization infers the application of constraints to the estimates of the autocorrelation functions. The constraints usually deal with how the data changes over time and space by constraining the energy of the ACFs or its derivative. This has an advantage of being more computationally tractable in that it is now a linear inverse problem. Using the ideas stated in this paper one can cast the reconstruction of the four dimensional function of the ACFs in these terms. The issue with doing this data based reconstruction is it is unknown how to constrain the reconstruction in the best way.

The two examples of data based regularization in the one dimensions ISR literature are lag profile inversion and deconvolution methods. Lag profile inversion creates an operator that takes the measured data from a theoretical ACFs to the measured ACFs [Virtanen *et al.*, 2008]. Along with the operator there is also an assumed Gaussian error. This error can be then estimated from the data. This Bayesian frame work can actually be rewritten as a least squares minimization along with a Tikhonov constraint. Because of this one can show that the deconvolution methods from Nikoukar *et al.* [2008] have almost the same structure as lag profile inversion.

With this in mind one can go a step further and investigate super resolution methods seen in image processing literature [Takeda *et al.*, 2009],[Takeda and Milanfar, 2011]. With these techniques along with the data regularization based framework in one dimensional ISR these techniques could be used to reconstruct the ACFs. This would require a complete change in the methodology in which 3-D ISR data is investigated. Basically instead of fitting data in the coordinate space of the radar we would first re-grid the data in a Cartesian space and then apply the nonlinear fitting. This would have the advantage of working with a linear inverse problem but the issues would be the same as with other data based regularization techniques were there is a question of what type of constraint should be used as opposed to a straight forward physical constraint.

5. Conclusion

We have presented a new method for analyzing incoherent scatter radar processing through use of the full space-time ambiguity function. This allows for taking into account the antenna beam pattern, pulse pattern and time integration. Through simulation we have shown how plasma motion can impact reconstruction of parameters which compounded with the non-linear nature of the parameter fitting step can create errors which are hard to predict. Lastly we have suggested a number of ways using three dimensional ISR systems we could mitigate these errors and reconstruct parameters at higher resolutions than what is currently possible.

Appendix A: Derivation of Idealized AMISR Array Pattern

The current antenna on the AMISR systems is made up 8x16 set of panel of half wave cross dipoles. Each panel has 32 cross dipoles in a 8x4 hexagonal configuration. In the current set up at the Poker Flat site this yields at 4096 element array in a 64x64 element hexagonal configuration.

In order to simplify the antenna can be treated as two rectangular arrays of cross dipoles interleaved together. In the x direction each of these arrays will have a spacing of $2d_x$ with $M/2$ elements. The y direction will be of length N elements and spacing d_y . Using basic planar phase array theory, [Balanis, 2005], we can start with the linear array pattern from the first array can be represented as

$$E_1(\theta, \phi) = \sum_{m=1}^{M/2} \sum_{n=1}^N e^{-j2(m-1)kd_x \sin \theta \cos \phi - j(n-1)kd_y \sin \theta \sin \phi}. \quad (\text{A1})$$

Since the second array can be thought of a shifted version of the first in the x direction we get the following

$$E_2(\theta, \phi) = \sum_{m=1}^{M/2} \sum_{n=1}^N e^{-j(2m-1)kd_x \sin \theta \cos \phi - j(n-1/2)kd_y \sin \theta \sin \phi}. \quad (\text{A2})$$

In order to simplify notation we will make the following substitutions, $\psi_x = -kd_x \sin \theta \cos \phi$, $\psi_y = -kd_y \sin \theta \sin \phi$. Using Equations A1 and A2 we can see the following relationship,

$$E_2(\theta, \phi) = e^{j(\psi_y/2 + \psi_x)} E_1(\theta, \phi) = \sum_{m=1}^{M/2} \sum_{n=1}^N e^{-j2(m-1)\psi_x - j(n-1)\psi_y}. \quad (\text{A3})$$

327 Adding E_1 and E_2 together we get the following linear array pattern

$$\begin{aligned}
 E(\theta, \phi) &= (1 + e^{j(\psi_y/2 + \psi_x)}) \sum_{m=1}^{M/2} \sum_{n=1}^N e^{-j2(m-1)\psi_x - j(n-1)\psi_y}. \\
 &= \frac{1}{MN} (1 + e^{j(\psi_y/2 + \psi_x)}) \frac{\sin((M/2)\psi_x)}{\sin(\psi_x)} \frac{\sin((N/2)\psi_y)}{\sin(\psi_y/2)}.
 \end{aligned}
 \tag{A4}$$

328 Since the array is steerable this can be taken into account in the equations by
 329 simply changing the definitions of ψ_x and ψ_y to $\psi_x = kd_x(\sin \theta \cos \phi - \sin \theta_s \cos \phi_s)$,
 330 and $\psi_y = kd_y(\sin \theta \sin \phi - \sin \theta_s \sin \phi_s)$. Lastly the antenna pattern of a single cross
 331 dipole can be represented as $\frac{1}{2}(1 + \cos(\theta)^2)$ [Balanis, 2005]. By taking the squared
 332 magnitude of the array factor and multiplying it with the pattern of the dipole we
 333 get Equation 11,

$$F(\theta_s, \phi_s, \theta, \phi) = \frac{1}{2}(1 + \cos(\theta)^2) \left| \frac{1}{MN} (1 + e^{j(\psi_y/2 + \psi_x)}) \frac{\sin((M/2)\psi_x)}{\sin(\psi_x)} \frac{\sin((N/2)\psi_y)}{\sin(\psi_y/2)} \right|^2.
 \tag{A5}$$

References

- 334 (2005), Eiscat 3d design specification document.
- 335 (2014), Amisr overview.
- 336 Balanis, C. A. (2005), *Antenna Theory: Analysis and Design*, Wiley-Interscience.
- 337 Butler, T. W. (2013), Spatial statistics and analysis of Earth's ionosphere, Ph.D.
 338 thesis.
- 339 Butler, T. W., J. Semeter, C. J. Heinselman, and M. J. Nicolls (2010), Imaging f
 340 region drifts using monostatic phased-array incoherent scatter radar, *Radio Sci.*,

45(5), RS5013, doi:10.1029/2010RS004364.

Dahlgren, H., J. L. Semeter, K. Hosokawa, M. J. Nicolls, T. W. Butler, M. G. Johnsen, K. Shiokawa, and C. Heinselman (2012a), Direct three-dimensional imaging of polar ionospheric structures with the resolute bay incoherent scatter radar, *Geophysical Research Letters*, 39(5), n/a–n/a, doi:10.1029/2012GL050895.

Dahlgren, H., G. W. Perry, J. L. Semeter, J. P. St. Maurice, K. Hosokawa, M. J. Nicolls, M. Greffen, K. Shiokawa, and C. Heinselman (2012b), Space-time variability of polar cap patches: Direct evidence for internal plasma structuring, *Journal of Geophysical Research: Space Physics*, 117(A9), A09,312, doi:10.1029/2012JA017961.

Dougherty, J. P., and D. T. Farley (1960), A theory of incoherent scattering of radio waves by a plasma, *Proceedings of the Royal Society of London. Series A, Mathematical and Physical Sciences*, 259(1296), pp. 79–99.

Dougherty, J. P., and D. T. Farley (1963), A theory of incoherent scattering of radio waves by a plasma, 3 scattering in a partly ionized gas, *Journal of Geophysical Research*, 68, 5473.

Farley, D. T. (1969), Incoherent scatter correlation function measurements, *Radio Sci.*, 4(10), 935–953.

Farley, D. T., J. P. Dougherty, and D. W. Barron (1961), A theory of incoherent scattering of radio waves by a plasma ii. scattering in a magnetic field, *Proceedings of the Royal Society of London. Series A, Mathematical and Physical Sciences*, 263(1313), pp. 238–258.

- 363 Gordon, W. (1958), Incoherent scattering of radio waves by free electrons with appli-
364 cations to space exploration by radar, *Proceedings of the IRE*, *46*(11), 1824–1829,
365 doi:10.1109/JRPROC.1958.286852.
- 366 Gray, R. W., and D. T. Farley (1973), Theory of incoherent-scatter measurements
367 using compressed pulses, *Radio Sci.*, *8*(2), 123–131, doi:10.1029/RS008i002p00123.
- 368 Hagfors, T. (1961), Density fluctuations in a plasma in a magnetic field, with ap-
369 plications to the ionosphere, *Journal of Geophysical Research*, *66*(6), 1699–1712,
370 doi:10.1029/JZ066i006p01699.
- 371 Holt, J. M., D. A. Rhoda, D. Tetenbaum, and A. P. van Eyken (1992), Opti-
372 mal analysis of incoherent scatter radar data, *Radio Sci.*, *27*(3), 435–447, doi:
373 10.1029/91RS02922.
- 374 Hysell, D. L., F. S. Rodrigues, J. L. Chau, and J. D. Huba (2008), Full profile
375 incoherent scatter analysis at jicamarca, *Annales Geophysicae*, *26*(1), 59–75, doi:
376 10.5194/angeo-26-59-2008.
- 377 Kudeki, E. (2003), *ECE 458 Lecture Notes, Application to Radio Wave Propagation*,
378 Univ. Of Illinois, Urbana IL.
- 379 Lehtinen, M. S. (1989), On optimization of incoherent scatter measurements, *Ad-
380 vances in Space Research*, *9*(5), 133 – 141, doi:http://dx.doi.org/10.1016/0273-
381 1177(89)90351-7.
- 382 Lehtinen, M. S., and I. Haggstrom (1987), A new modulation principle for incoherent
383 scatter measurements, *22*, 625–634, doi:10.1029/RS022i004p00625.

- Lehtinen, M. S., and A. Huuskonen (1996), General incoherent scatter analysis and {GUIDAP}, *Journal of Atmospheric and Terrestrial Physics*, 58(1–4), 435 – 452, doi:http://dx.doi.org/10.1016/0021-9169(95)00047-X, Selected papers from the sixth international Eiscat Workshop.
- Lehtinen, M. S., A. Huuskonen, and J. Pirttilä (1997), First experiences of full-profile analysis with GUIDAP, *Annales Geophysicae*.
- Nicolls, M. J., and C. J. Heinselman (2007), Three-dimensional measurements of traveling ionospheric disturbances with the Poker Flat Incoherent Scatter Radar, *Geophysical Research Letters*.
- Nikoukar, R. (2010), Near-optimal inversion of incoherent scatter radar measurements- coding schemes, processing techniques, and experiments, Ph.D. thesis, University of Illinois at Urbana-Champaign.
- Nikoukar, R., F. Kamalabadi, E. Kudeki, and M. Sulzer (2008), An efficient near-optimal approach to incoherent scatter radar parameter estimation, *Radio Science*, 43(5), n/a–n/a, doi:10.1029/2007RS003724.
- Richards, M. A. (2005), *Fundamentals of Radar Signal Processing*, McGraw-Hill.
- Semeter, J., T. Butler, C. Heinselman, M. Nicolls, J. Kelly, and D. Hampton (2009), Volumetric imaging of the auroral ionosphere: Initial results from pfisr, *Journal of Atmospheric and Solar-Terrestrial Physics*, 71, 738 – 743, doi:10.1016/j.jastp.2008.08.014, Advances in high latitude upper atmospheric science with the Poker Flat Incoherent Scatter Radar (PFISR).

- 405 Sulzer, M. P. (1989), Recent incoherent scatter techniques, *Advances in Space Re-*
406 *search*, *9*, 153–162, doi:10.1016/0273-1177(89)90353-0.
- 407 Sulzer, M. P. (1993), A new type of alternating code for incoherent scatter measure-
408 ments, *Radio Science*, *28*(6), 995–1001, doi:10.1029/93RS01918.
- 409 Takeda, H., and P. Milanfar (2011), Removing Motion Blur With Space-Time Pro-
410 cessing, *Image Processing, IEEE Transactions on*, *20*(10), 2990–3000.
- 411 Takeda, H., P. Milanfar, M. Protter, and M. Elad (2009), Super-Resolution Without
412 Explicit Subpixel Motion Estimation, *Image Processing, IEEE Transactions on*,
413 *18*(9), 1958–1975.
- 414 Virtanen, I. I., M. S. Lehtinen, and T. Nygrén (2008), Lag profile inversion method
415 for EISCAT data analysis, *Annales*

416 **Acknowledgments.** (Text here)

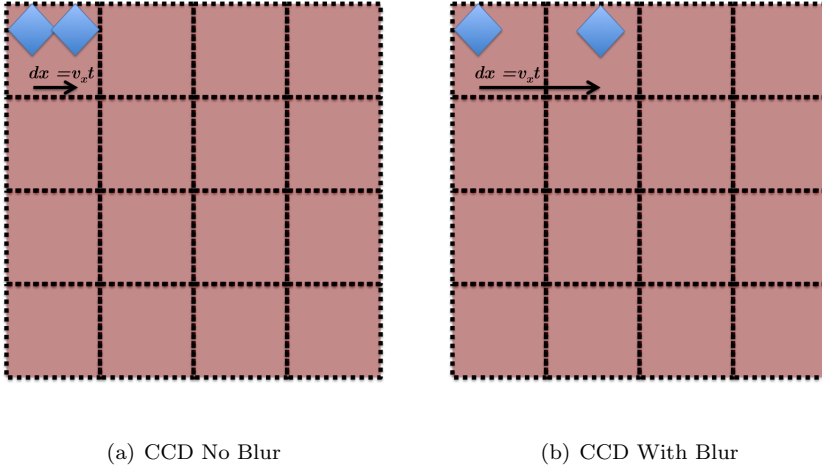


Figure 1. CCD camera

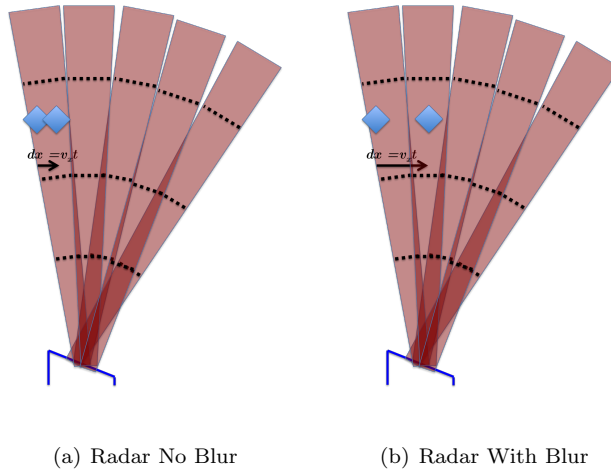


Figure 2. Radar

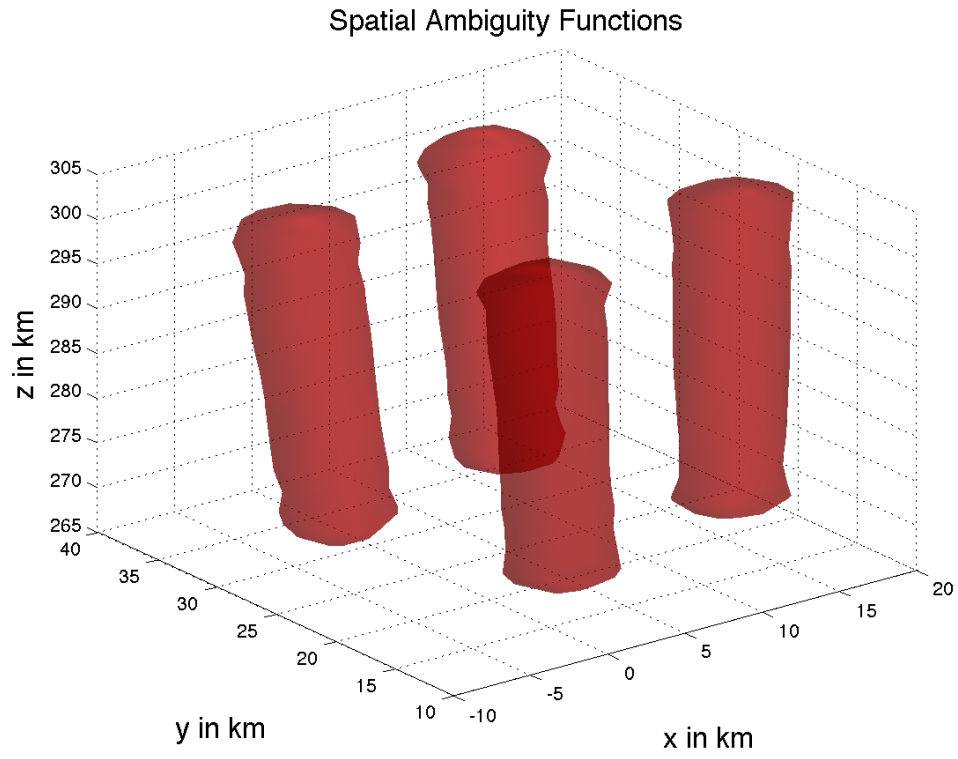


Figure 3. Full Spatial Ambiguity Function

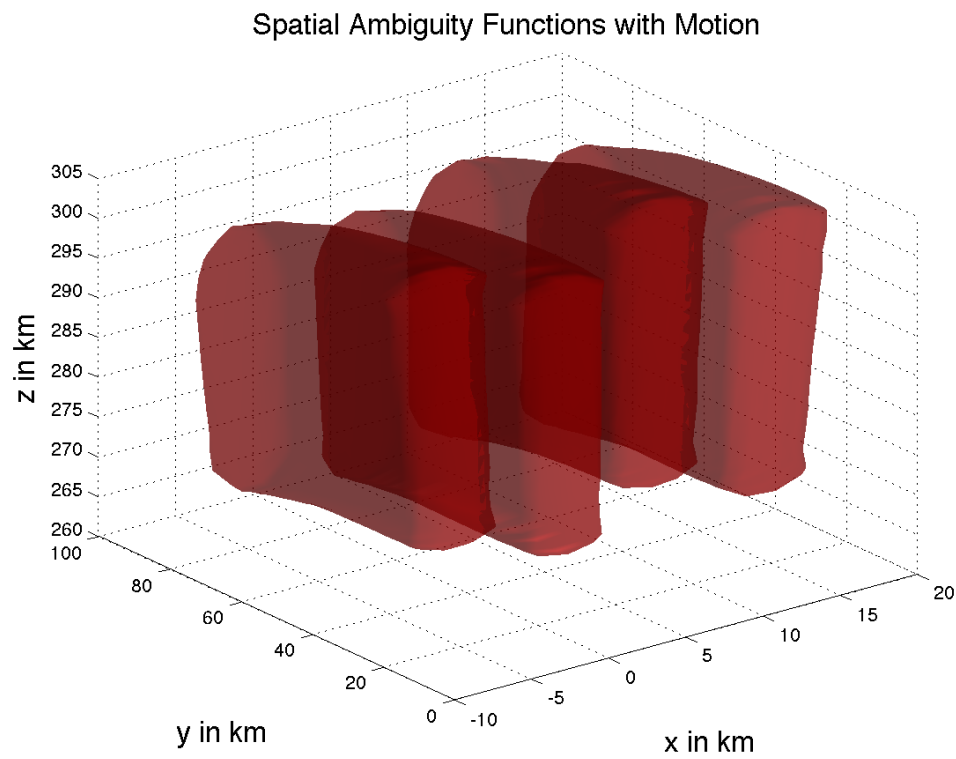


Figure 4. Full Spatial Ambiguity Function With Motion

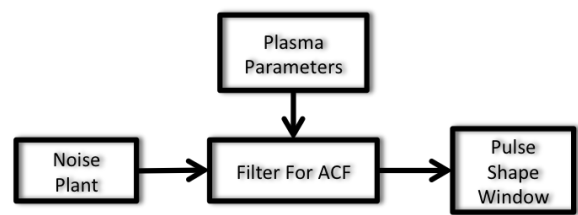


Figure 5. I/Q Simulator Diagram

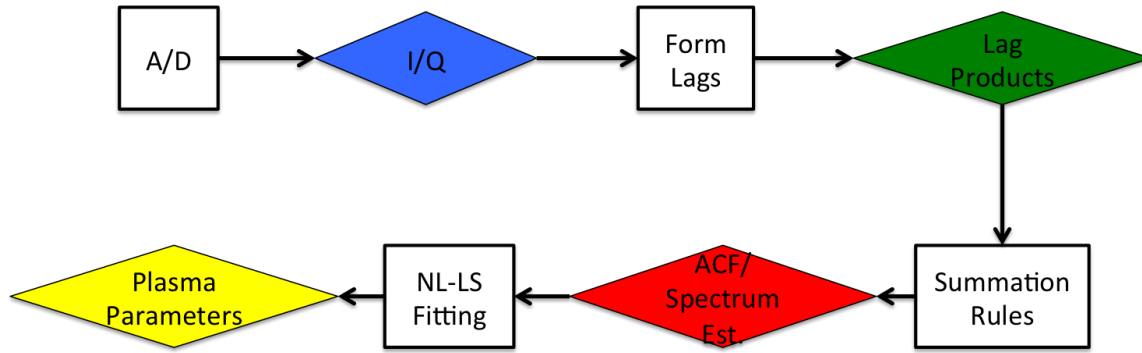


Figure 6. ISR Processing Chain.

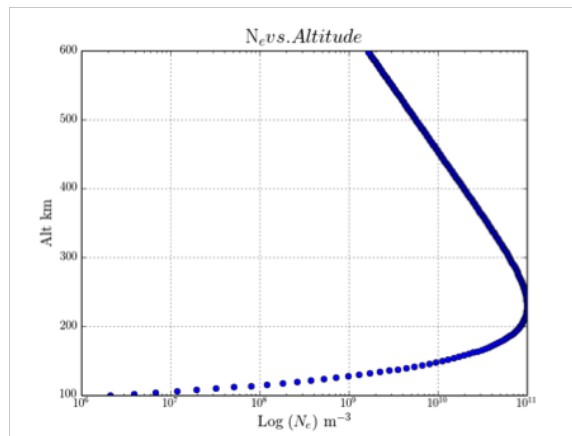


Figure 7. Electron density vs. altitude.

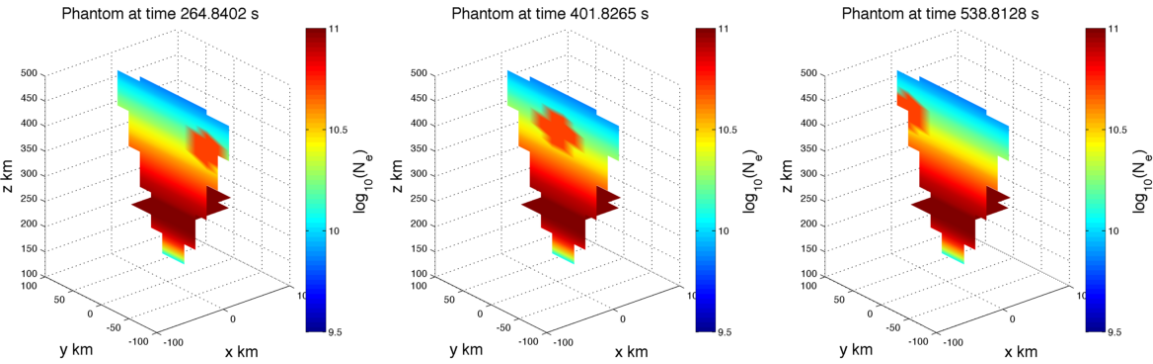


Figure 8. Example images from phantom

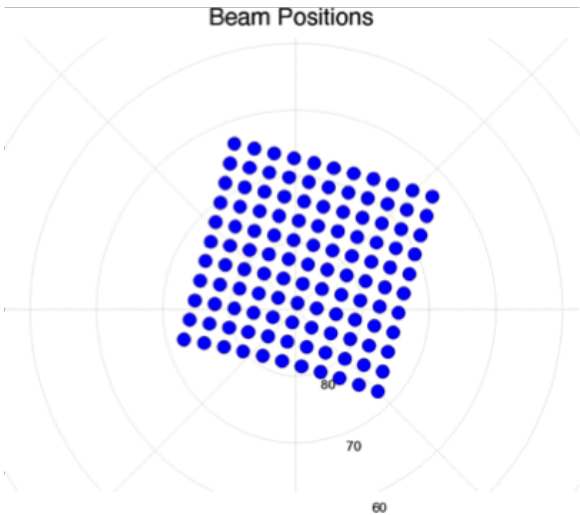


Figure 9. Beam pattern

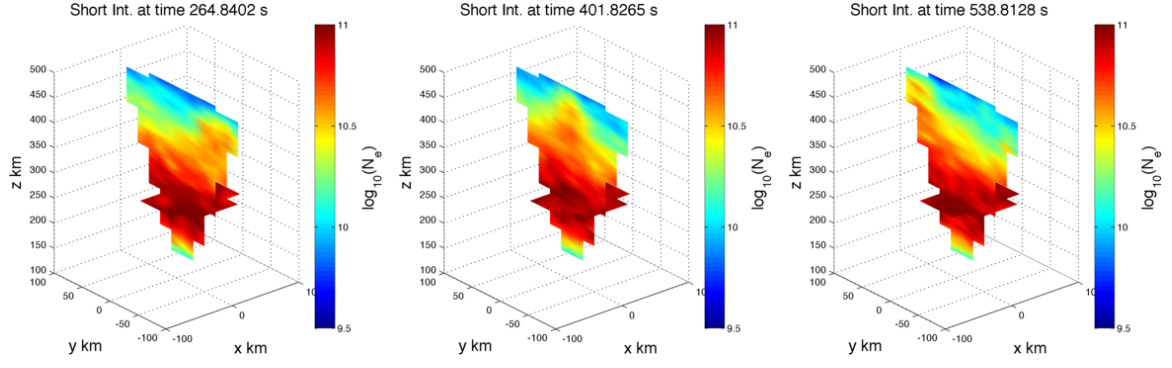


Figure 10. Example images from variable data

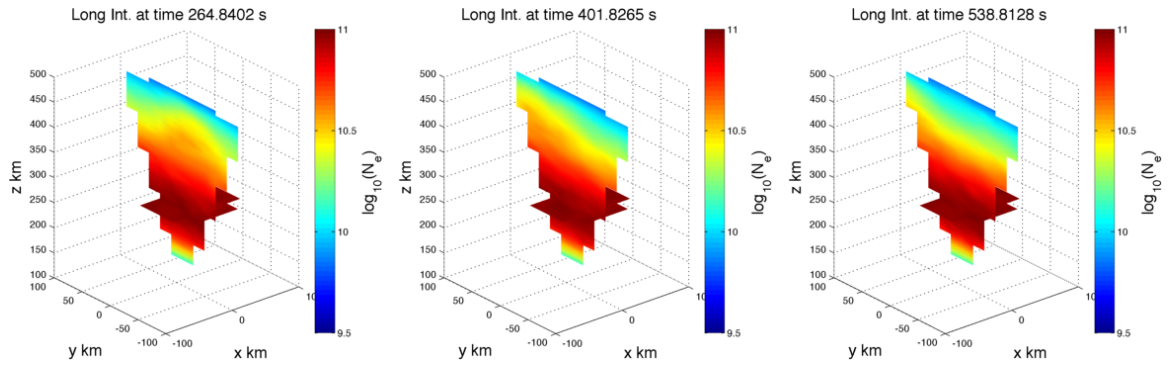


Figure 11. Example images from blurred data

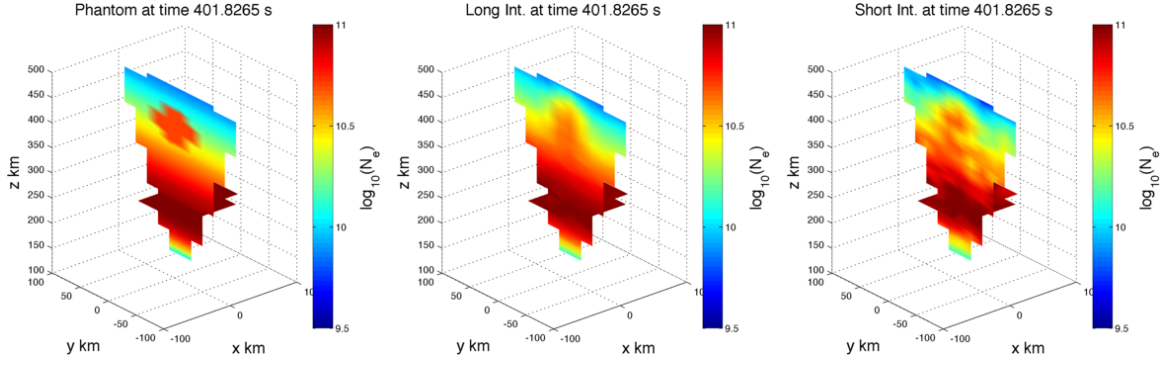


Figure 12. Stationary phantom along with both types of reconstructions.

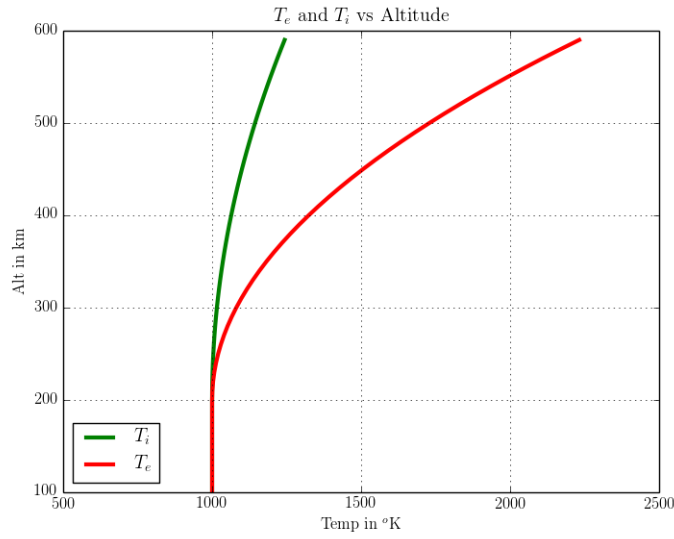


Figure 13. Ion & electron temperature vs. height.

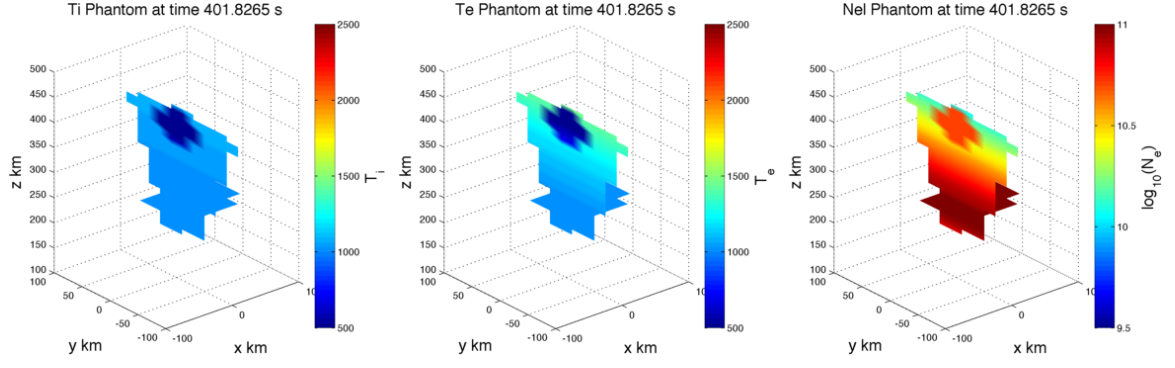


Figure 14. Phantom of parameters.

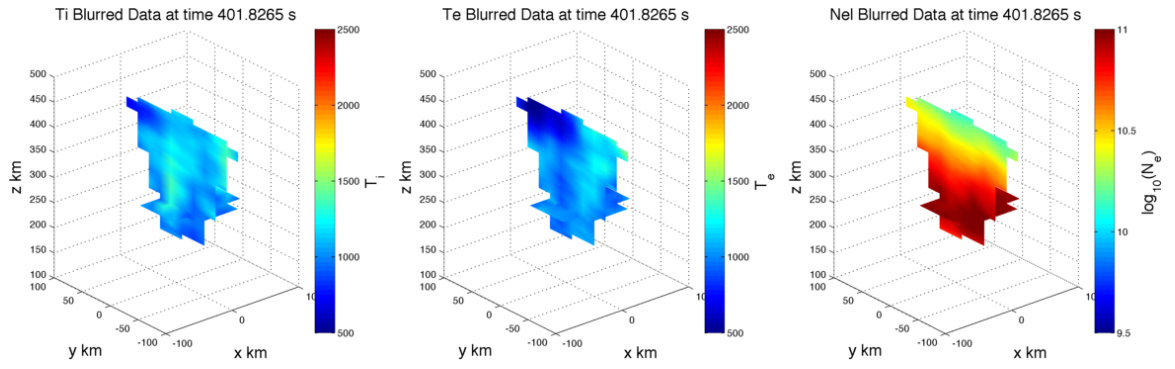


Figure 15. Blurred data after full fitting.